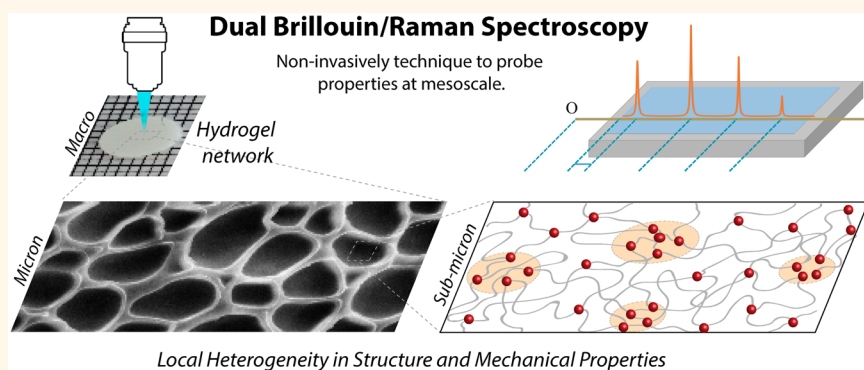


Assessment of Local Heterogeneity in Mechanical Properties of Nanostructured Hydrogel Networks

Zhaokai Meng,[†] Teena Thakur,[†] Chandani Chitrakar,[†] Manish K. Jaiswal,[†] Akhilesh K. Gaharwar,^{*,†,‡,§,||} and Vladislav V. Yakovlev^{*,†,||}

[†]Department of Biomedical Engineering, [‡]Department of Materials Science and Engineering, [§]Center for Remote Health Technologies and Systems, and ^{||}Department of Physics and Astronomy, Texas A&M University, College Station, Texas 77843, United States

S Supporting Information



ABSTRACT: Our current understanding of the mechanical properties of nanostructured biomaterials is rather limited to invasive/destructive and low-throughput techniques such as atomic force microscopy, optical tweezers, and shear rheology. In this report, we demonstrate the capabilities of recently developed dual Brillouin/Raman spectroscopy to interrogate the mechanical and chemical properties of nanostructured hydrogel networks. The results obtained from Brillouin spectroscopy show an excellent correlation with the conventional uniaxial and shear mechanical testing. Moreover, it is confirmed that, unlike the macroscopic conventional mechanical measurement techniques, Brillouin spectroscopy can provide the elasticity characteristic of biomaterials at a mesoscale length, which is remarkably important for understanding complex cell–biomaterial interactions. The proposed technique experimentally demonstrated the capability of studying biomaterials in their natural environment and may facilitate future fabrication and inspection of biomaterials for various biomedical and biotechnological applications.

KEYWORDS: nanostructured hydrogels, mechanical properties, microscopy, nanoparticles, Brillouin spectroscopy

Unparalleled challenge exists in designing the next generation of mechanically resilient biomaterials for recently emerging biomedical applications, including regenerative medicine, cancer research, bioenergy, bioelectronics, and medical diagnostics.^{1,2} However, conventional mechanical tests, either macroscopic techniques such as shear rheology or microscopic approaches such as atomic force microscopy, require forces to be applied on the biomaterials' surface. Therefore, those techniques may not be suitable for real-time and continuous measurements.^{3–5} Noncontact elastography, on the other hand, is usually limited by their spatial resolution and is inadequate for microscopic or mesoscopic assessment.^{6–8} Clearly, there is a pressing need

for a noncontact and reliable mechanical testing method capable of filling the existing technology gap.

In this report, we demonstrate the capabilities of recently developed dual Brillouin/Raman microspectroscopy to simultaneously interrogate the mechanical and chemical properties of hydrogel networks. This technique opens an opportunity to interrogate physicochemical properties of biomaterials and cell–matrix interactions *in situ*. Specifically, this technique demonstrates local heterogeneity within nanostructured hydrogels, which up until now researchers only speculated. Our

Received: December 20, 2016

Accepted: July 18, 2017

Published: July 26, 2017



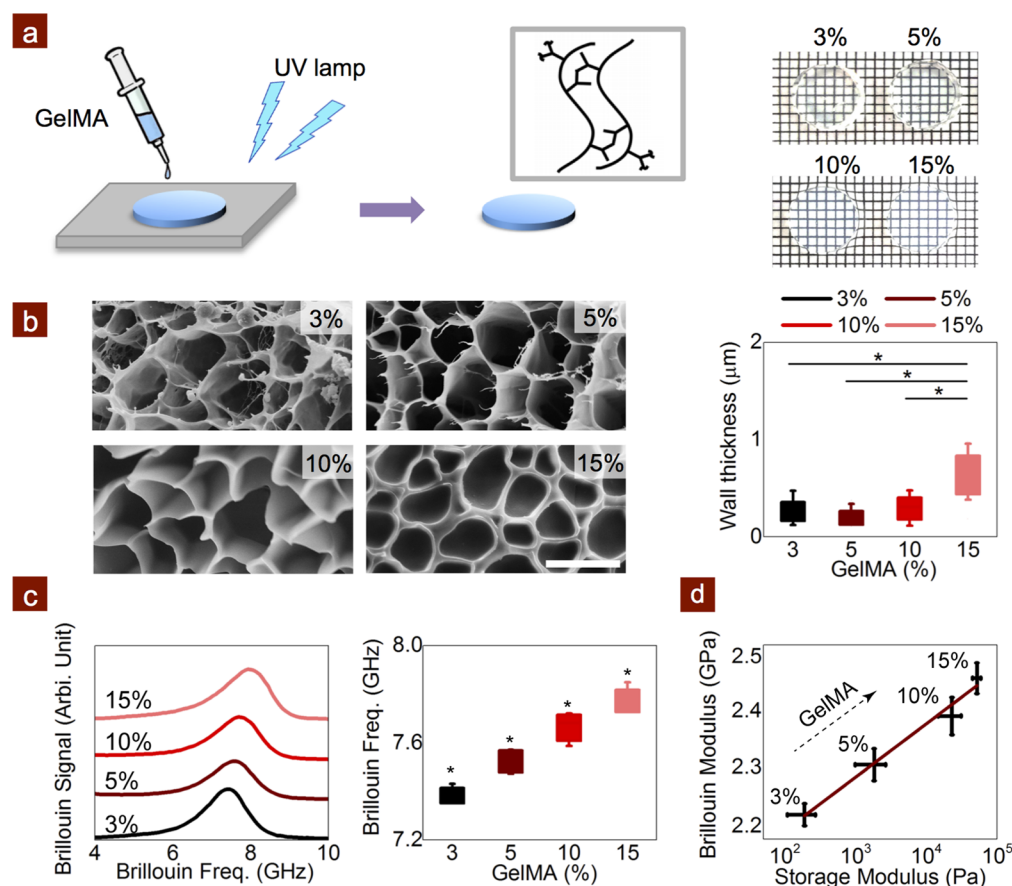


Figure 1. Investigating mechanical properties of polymeric hydrogel using Brillouin spectroscopy. (a) Covalently cross-linked hydrogels were fabricated from gelatin methacrylate (GelMA) by exposing the prepolymer solution to UV radiation. The images show optical characteristics of hydrogels with increasing GelMA concentration. (b) Scanning electron microscopy images indicate the presence of a highly porous and interconnected network in dried hydrogels (scale bar = 10 μm). The increase in GelMA concentration results in an increase in the pore wall thickness (* $p < 0.05$). (c) Brillouin spectra of hydrogels with different GelMA concentration. The effects of GelMA concentration on Brillouin signal and frequency are shown (* $p < 0.05$). (d) Positive correlation between the Brillouin moduli and the storage/loss moduli was observed.

approach provides experimental evidence that local heterogeneity exists in biomaterials at a mesoscale length.

As a viscoelasticity-specific optical technique, spontaneous Brillouin spectroscopy has been utilized for material characterizations.^{9–14} Inelastic interactions between the incident electromagnetic wave and the intrinsic thermal phonons of the material results in Brillouin scattering. Due to these interactions, the incident electromagnetic wave experiences a frequency shift, which is associated with the material's sound speed or longitudinal/viscous modulus. Once this frequency shift is determined *via* experiment, the longitudinal and viscous moduli can be derived accordingly (longitudinal modulus: $E' = \frac{\rho \lambda^2 \nu_B^2}{4n^2}$, viscous modulus: $E'' = \frac{\rho \lambda^2 \nu_B \Delta \nu_B}{4n^2}$). Here, ρ is the mass density of the material, λ is the incident wavelength, ν_B is the Brillouin shift, $\Delta \nu_B$ is the line width of the Brillouin shift, and n is the optical refractive index of the material.

Brillouin spectroscopy offers a nondestructive and non-contact approach with submicron spatial resolution to probe viscoelastic characteristics of materials when compared to other viscoelasticity-specific imaging techniques. In this sense, Brillouin spectroscopy can provide comprehensive understanding of the interactions between the biomaterials and the surrounding biological components.¹⁵ In this study, we utilize dual Brillouin/Raman approach to simultaneously obtain Raman and Brillouin spectra, without sacrificing the acquisition

time or system complexity. The Raman spectral signatures can be used to determine the chemical characteristics of the biomaterials, whereas the Brillouin signal can be used to assess mechanical characteristics of biomaterials.

Unlike Raman spectroscopy, which has been investigated extensively during the past decades, Brillouin spectroscopy faces many challenges in its instrumentations and applications. The main hurdles of practical Brillouin imaging/sensing are the long acquisition time and the strong background induced by elastic scatterings. Recently, we have advanced a background-free Brillouin spectroscopic analysis using a virtually imaged phased array (VIPA) and a CCD camera.^{15–17} The bleed-through elastic light scattering was successfully suppressed using an appropriate atomic/molecular absorption filter. We have also incorporated a Raman spectroscopy detection channel into the Brillouin microscope, making dual Brillouin/Raman sensing/imaging possible.¹⁵

The spatial resolution of Brillouin spectroscopy allows one to probe the mechanical characteristics of biomaterials at the mesolength scale. It is important to measure properties at mesolength scale because repair and regeneration of damaged tissues fall between micro- and macrolength scale. For example, biomaterials' surface dictates foreign body reactions, and fibrosis, cell–cell interactions, and cell–matrix interactions have been shown to control and regulate neo-tissue formation, which are all mesoscopic phenomena. Simultaneous inves-

tigation of both chemical and mechanical properties of biomaterials in a nondestructive manner can be used to interrogate the cell–biomaterial interactions over an extended period. Moreover, it is also possible to monitor the resorption of biomaterials and tissue in-growth within the biomaterial scaffold using Brillouin spectroscopy. The properties of materials will influence the Brillouin shift and Brillouin line width, so it is important to calibrate the system to specific biomaterials or tissue type. In addition, a nondestructive and noncontact approach of Brillouin spectroscopy can be used for *in situ* assessments of the mechanical properties during biomanufacturing and 3D printing.

RESULTS AND DISCUSSION

We first synthesized covalently cross-linked hydrogels from denatured collagen (gelatin) to mimic different tissue stiffness (Figure 1a). Photo-cross-linkable gelatin methacrylate (GelMA) was obtained by modifying the amine groups present on the gelatin backbone with methacrylic anhydride, according to our previous reports.^{18–20} GelMA hydrogels have many of the features of native extracellular matrix, including cell attachment and matrix protease-responsive peptide motifs, as well as elastic mechanical properties that can be tuned *via* cross-linking, making them appealing materials for engineered tissues. Further, GelMA hydrogels can be microfabricated using various methodologies such as photolithography, bioprinting, self-assembly, and microfluidic techniques to generate constructs with controlled composite architectures. We and others have shown that GelMA mechanical properties can be further tuned through the addition of nanoparticles that influence the sensitivity of attached cells to mechanical stimuli, including material stiffness and dynamic loading.^{20–23} To mimic biomechanical properties of tissue structures, we selected different concentrations of covalently cross-linked GelMA hydrogels (3, 5, 10 and 15% w/v). The structural and mechanical properties of these polymeric hydrogels were investigated and correlated with Brillouin and Raman spectra. The optical instrumentation used in those experiments is shown in Figures S1 and S2.

We captured the microscopic morphology of the dried hydrogels using scanning electron microscopy (SEM). All the covalently cross-linked hydrogels (dried) exhibited a porous and interconnected network (Figure 1b). The pore sizes range from 3 to 10 μm among all the samples (Figure S4a). Interestingly, the wall thickness of the pores showed a positive correlation with the polymer concentration. The increase in wall thickness is attributed to higher wt % of polymer in the hydrogel network that results in enhanced cross-linking. The increase in cross-linking density reinforces the hydrogel network and results in an increase in mechanical stiffness.

Next, we assessed the viscoelastic properties and chemical characteristics of the hydrogel network using the dual Brillouin/Raman system. Examples of the Brillouin spectra are illustrated in Figure 1c. A typical Brillouin spectrum consists of three peaks: an elastic peak located in the center and two Brillouin peaks, representing the Stokes and anti-Stokes components, located on the left and the right side of the elastic peak. The quantitative information can be extracted from the spectrum according to the position and the line shape of the Brillouin peaks (see Supporting Information and the Determination of Brillouin Shift section). We utilized an iodine cell as a narrow-band notch filter¹⁶ to minimize the unwanted elastic signal that was bleeding through the spectrometer. The absorption cell can

distort the line shape of the Brillouin peaks (see Supporting Information). For example, in Figure 1c, the anti-Stokes part of the Brillouin spectrum was partially absorbed by the iodine cell. However, by carefully taking those sudden features into account, we were able to retrieve the position of Brillouin lines with an accuracy of ± 1 MHz.²⁴

The sampling points were randomly selected across the hydrogel samples. Although heterogeneity can be revealed by SEM images, the Brillouin shift was almost insensitive to the position across the samples. We attribute this observation to a relatively large light–matter interaction volume defined by our optical system. In our case, according to the numerical aperture of the objective lens ($\text{NA} = 0.25$), a typical focal volume was $\sim 2.6 \times 2.6 \times 8.5 \mu\text{m}^3$ (for a focusing lens with the $\text{NA} = 0.25$), which is sufficient to cover an average-sized pore and its surrounding walls. In this sense, the Brillouin scattering signal was induced by both the walls and the pores. Nevertheless, the Brillouin shifts/moduli show sensitivity to the GelMA's concentration.

The Stokes peaks are zoomed in for better comparison (Figure 1c) to emphasize the relationship between the Brillouin shift and the hydrogel concentrations. In order to quantify the correlation between Brillouin shift/modulus and the GelMA concentration, we performed at least 25 measurements on five different hydrogels. A positive correlation between the Brillouin shift and the polymer concentrations was observed (Figure 1c). Nevertheless, the Brillouin line width, which is associated with the viscous properties of hydrogel network, does not strictly correlate with the GelMA concentration (Figure S4d).

In this study, we also utilized conventional mechanical testing (shear rheology) to characterize the quasi-static mechanical properties of the hydrogel network and to validate data obtained from Brillouin spectroscopy. The viscoelastic properties of the hydrogel network derived from the shear rheology technique can be described by the storage modulus (E'_s) and the loss modulus (E''_s). Here, the subscript “S” denotes that the moduli are measured by static/quasi-static techniques. Both the storage and loss moduli of the polymeric network exhibit a positive association with the GelMA concentration (Figures 1d and S5). This is expected, as the increased GelMA concentration results in enhanced cross-linking density. Moreover, the increase of the wall thickness of the hydrogel network also contribute to the elevated stiffness.

The positive association between the shear moduli and Brillouin moduli is illustrated in Figure 1d. Here, we treated cross-linked hydrogels as aqueous solution filled with collagen fibers. Following previous studies, the index-density factor ρ/n^2 for the hydrogel is expected to be a constant ($\rho/n^2 = 1.57 \text{ g/cm}^3$).²⁵ Unlike quasi-static techniques such as compression or shear rheology, Brillouin spectroscopy provides the elastic modulus of the hydrogel network in the high-frequency regime ($\sim 1\text{--}10 \text{ GHz}$). This is mainly attributed to the acoustic dispersion of the hydrogel network. For example, the longitudinal modulus obtained from Brillouin spectra is orders of magnitude higher than those obtained from quasi-static analytical techniques. Conventional elastic moduli can be correlated with Brillouin moduli using $E'_b = 10^b (E'_s)^a$,²⁶ where E'_b and E'_s are the Brillouin and quasi-static elastic moduli, respectively. Both “a” and “b” are material-dependent coefficients, and we have taken $a = 8.3059 \pm 0.0003$ and $b = 0.0175 \pm 0.0013$ for our calculations. Overall, the results identified in Figure 1d confirmed that the elasticity of hydrogels

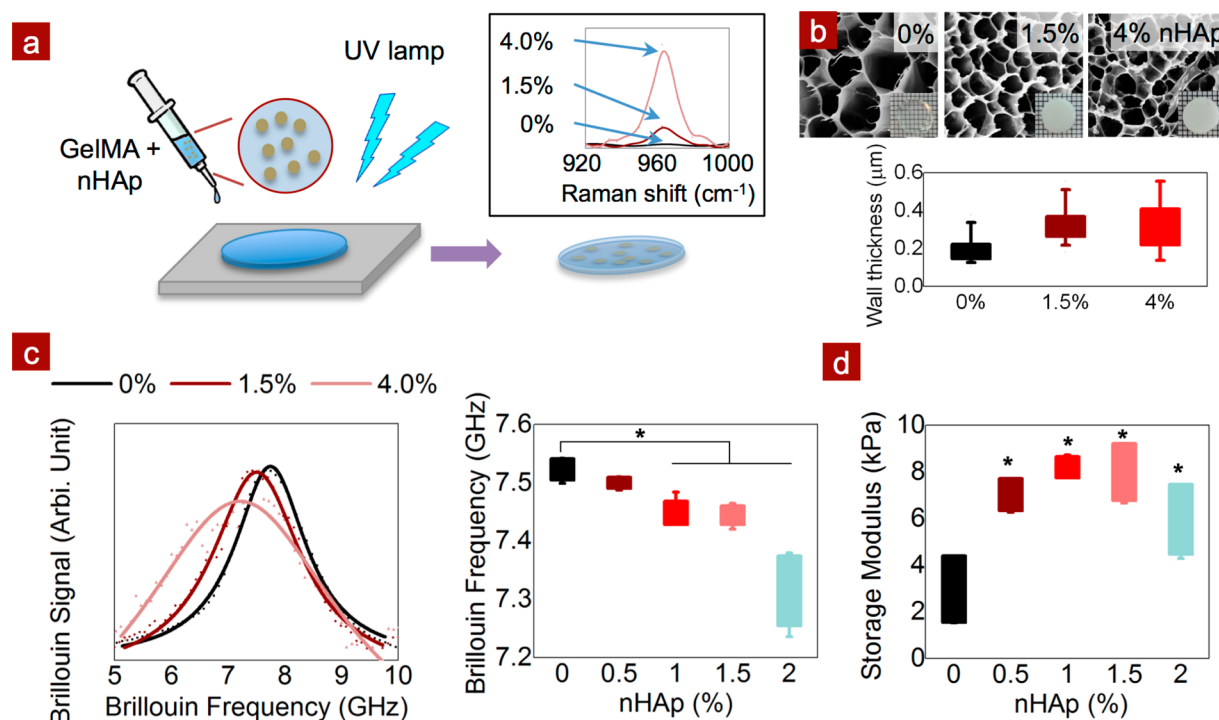


Figure 2. Investigating mechanical properties of nanoengineered hydrogels using Brillouin spectroscopy. (a) Fabrication process of nanocomposite hydrogels. Inset shows Raman spectra, confirming the presence of nHAp ($\sim 960\text{ cm}^{-1}$, indicator of PO_4^-). (b) SEM images for nanocomposites with different nHAp concentrations and its effect on the wall thickness. The optical transparency of hydrogels is reduced due to addition of nHAp, as shown in the insets. (c) Brillouin spectra and frequency as a function of nHAp concentration ($*p < 0.05$). (d) Correlation between the Brillouin spectroscopy results and the rheology measurements ($*p < 0.05$).

network can be assessed using Brillouin spectroscopy in a nondestructive manner.

To further extend the applicability of Brillouin spectroscopy toward mineralized tissues, we fabricated nanocomposite hydrogels loaded with hydroxyapatite nanoparticles (nHAp) and covalently cross-linked GelMA hydrogels. nHAp is present in mineralized tissues such as bone, dental enamel, and dentin. We combined nHAp (0–4% w/v) with the GelMA prepolymer solution prior to the photo-cross-linking procedure to mimic mineralized tissue (Figure 2a). The microstructures of nanocomposite hydrogels were characterized using SEM (Figure 2b). The microscopic morphology, including the wall thickness and the pore size of nanocomposite hydrogels (Figures 2b and S6a). We did not observe any significant change in pore size and pore thickness due to addition of nHAp to GelMA. This might be due to limited interactions between nHAp and GelMA, similar to previously reported studies.²⁰ To validate the presence of nHAp within the hydrogel network, we analyzed Raman spectra for the nanocomposite hydrogels (Figures 2a and S6b,c). Due to the strong autofluorescence emissions from the samples, we only concentrate on Raman peaks for phosphate ($\nu_1\text{ PO}_4^- \sim 960\text{ cm}^{-1}$) contributed by nHAp, C–H bonds ($2600\text{--}3000\text{ cm}^{-1}$) contributed by GelMA, and O–H bonds ($\sim 3100\text{--}3400\text{ cm}^{-1}$) originating from surrounding water molecules. Among the nanocomposite samples, we identified a positive association between the nHAp concentration and the phosphate peak (960 cm^{-1}) strength. At higher nHAp concentrations ($>3\text{ wt } \%$), the strength of all Raman peaks was reduced due to the increased turbidity of the sample. The use of Raman along with Brillouin can be used to simultaneously determine extracellular matrix remodeling and formation of mineralized tissue.

The Brillouin spectra of the nHAp-reinforced hydrogels were recorded and analyzed (Figure 2c). The presence of nHAp nanoparticles leads to a stronger elastic scattering (Figure S7), which makes it necessary to correct for elastic background scattering (Figures 2c and S7). Since the size of nanoparticles is substantially smaller than the probing volume in Brillouin microscopy, and the distribution of nanoparticles is considered to be random, we neither expected nor experimentally observed any additional resonances associated with those nanoparticles or their interaction with the surrounding medium. Once again, the Brillouin frequency shifts due to material characteristics can be precisely identified by detecting the center of Brillouin peaks. We also observed that the line width of the Brillouin peak was much broader than that of their pure GelMA counterparts (Figures 2c, S7 and S8), and the reduced accuracy of its determination was likely affected by the limited signal strength.

We observed a negative association between the nHAp concentration and the Brillouin shift (Figure 2d). These results suggested that the addition of nHAp to GelMA decreased elasticity of the hydrogel network at microscopic length scale. The quasi-static elastic modulus obtained by shear rheology demonstrates a positive correlation with nHAp concentration ($<2\%$) (Figures 2d and S8c,d). At higher nHAp concentration, no significant difference in storage and loss moduli was observed. This behavior is drastically different when compared to Brillouin measurements. According to the Brillouin shift, the addition of nHAp to GelMA reduces the Brillouin moduli. This contradiction can be explained in terms of the hydrogel networks' heterogeneity at different length scales. In the Brillouin microscopy studies, we only probed a local microscopic area confined by a focal region, whereas the shear

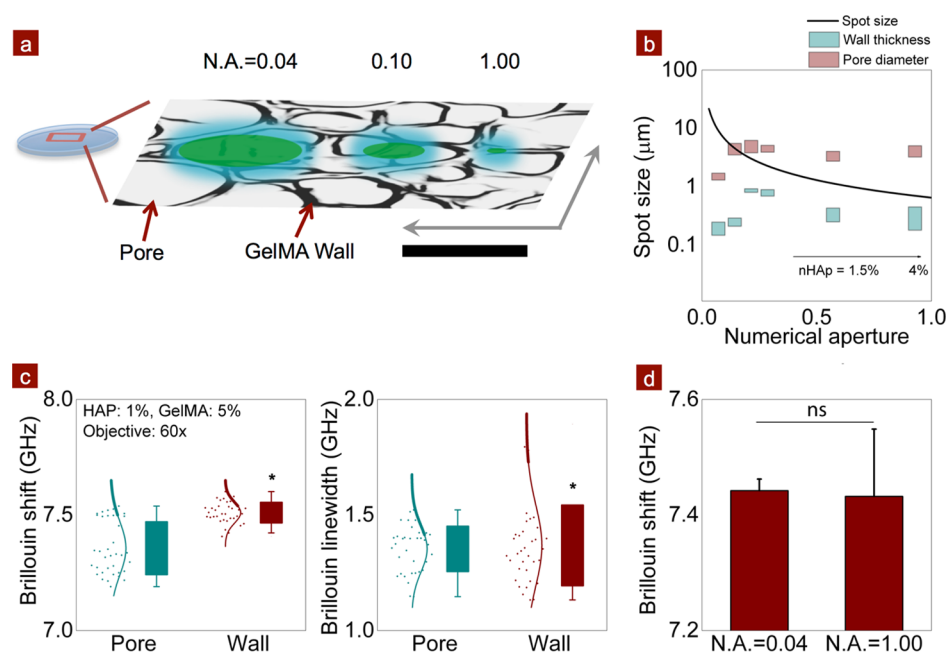


Figure 3. Assessment of local heterogeneity in mechanical properties of a bulk hydrogel network. (a) Illustration of the relationship between numerical aperture and the corresponding focusing spot size. (b) Solid line: the focusing spot size as a function of the numerical aperture of the objective lens. Boxes: the measured wall thickness for pure GelMA and GelMA + nHAp samples are plotted as a reference. The left four pairs of boxes are measured from pure GelMA samples, and the right three pairs of boxes are measured from nanocomposite hydrogel samples. (c) Brillouin shift and line width for spots randomly selected from the sample ($*p < 0.05$). The numerical aperture of the objective was 1.00. The focusing position was determined *via* the optical image simultaneously captured during the experiment by a separate camera. (d) Statistics results of the Brillouin shift acquired from random points with different objective lens ($*p < 0.05$). The results corresponding to the higher numerical aperture objective lens give a stronger fluctuation.

rheology technique investigates the hydrogel stiffness at macroscopic (~ 1 – 10 cm) length scale. These results suggest that the nanocomposite hydrogels show heterogeneous mechanical properties at different length scales.

To further elucidate the effect of the heterogeneity of the nanocomposite hydrogels, we acquired Brillouin shift using objective lenses with different numerical apertures. The spot size affects the interrogation volume (Figure 3a), and this is particularly important when probing inhomogeneous samples. To investigate the relationship between the spot size and Brillouin shift, we employed two objective lenses with distinct numerical apertures (NA = 0.04 and 1.00) (Figure 3b). Their corresponding focus spot sizes are $\sim 16 \times 16 \times 300$ and $\sim 0.6 \times 0.6 \times 0.5$ μm . Based on the SEM images (Figures 1b and 2b), it is expected that the larger spot size, which is affordable by a lower numerical aperture objective (NA = 0.04), will provide the averaged information over an area of $16 \mu\text{m}^2$, whereas the smaller spot size (NA = 1.00) with a spot size $< 1 \mu\text{m}$ will cover only a small fraction of the area (Figure 3a,b and Figure 2b). To validate this hypothesis, we randomly selected 36 points on nanocomposite hydrogels (1% nHAp). The acquired Brillouin shift results are plotted in Figures 3c and S9. When utilizing smaller focusing spot size, the values for Brillouin shift were widely distributed. The statistical comparison is given in Figure 3d. For the low NA (NA = 0.04) lens, the Brillouin shift was 7.4421 ± 0.0200 GHz and for the high-NA (NA = 1.00) lens, the Brillouin shift was 7.4322 ± 0.1164 GHz. The averaged Brillouin shift acquired by the two objective lenses did not exhibit significant difference ($p > 0.05$, Figure 3d). However, the standard deviations of these two data sets were different by approximately a factor of 5-fold. This indicates that the Brillouin shift is highly sensitive to the microscopic position in

the nanocomposite hydrogel networks, reflecting the heterogeneity of their mechanical properties. We note that the increase of the numerical aperture of the objective lens would cause a line-broadening effect in Brillouin spectroscopy. However, under the backscattering configuration that is adopted in our experiment, the absolute Brillouin shift is insensitive to the numerical aperture of the objective lens.²⁷

CONCLUSION

Overall, we have shown that dual Brillouin/Raman spectroscopy can be used to probe the mechanical and chemical properties of nanostructured hydrogel networks. The non-contact and noninvasive nature of Brillouin spectroscopy highlights its capabilities for *in situ* and *in vivo* applications, including monitoring tissue regeneration and diagnosing cancer. Specifically, we characterized the mechanical stiffness of pure and nanocomposite hydrogels using Brillouin spectroscopy. For the pure polymeric hydrogels, Brillouin shifts agreed with the storage modulus of the hydrogel network obtained *via* conventional techniques. Meanwhile, for hydrogels loaded with nanoparticles, a heterogeneous distribution of mechanical stiffness at micrometer length scale was observed. Unlike macroscopic characteristic techniques, Brillouin spectroscopy enables investigators to assess the viscoelasticity of the hydrogel at the mesoscale that ranges from submicron to tens of microns, which would help to better understand biomaterials' microscopic viscoelasticity. This technique can be used to determine the mechanical/chemical characteristics of a range of hydrogel biomaterials. Moreover, with the assistance of Raman measurement, investigators are able to monitor the chemical information on the sample without additional operations. The dual Brillouin/Brillouin spectroscopy may assist future

fabrication and *in situ* inspection of functional biomaterials in various biomedical applications.

EXPERIMENTAL SECTION

Preparation of Polymer Hydrogels and Nanocomposites.

Polymer hydrogels were prepared by covalently cross-linking them in the presence of UV light. Briefly, 3, 5, 10, and 15% GelMA were dissolved in 0.25% photoinitiator solution (Ciba IRGACURE 2959, Ciba Specialty-Chemical, USA) at 60 °C. The prepolymer mix was then subjected to UV exposure (320–500 nm) at an intensity of 1.44 W/cm² for 90 s to obtain covalently cross-linked hydrogels (Omnicure S200, Lumen Dynamics). Hydroxyapatite nanopowder purchased from Sigma-Aldrich, USA, was used to fabricate nanocomposite hydrogels. Briefly, 10% (w/v) solution of nHAp stock was prepared in distilled water and allowed to uniformly disperse under sonication for 15 min. A 5% (w/v) solution of GelMA was prepared in photoinitiator solution, and an appropriate volume of nHAp stock was added to make the final volume up to 0.5, 1, 1.5, 2, 2.5, 3, 3.5, and 4%. The nanocomposite solution was then cross-linked under UV exposure at 1.44 W/cm² for 90 s to obtain nanocomposite hydrogels.

Morphological Characterization of Hydrogels. Scanning electron microscopy was performed to study the pore size distribution and wall thickness of polymer hydrogels/nanocomposites. Samples for SEM characterization were frozen in liquid nitrogen prior to lyophilization for 36 h. Completely dried samples were broken with forceps to expose the cross section and mounted onto carbon-taped SEM stubs. Dried samples were sputter-coated with Au/Pd (~31 nm) prior to imaging under SEM (JEM 5000 SEM, Nikon Instruments) at an acceleration voltage of 10 kV. Pore size distribution and wall thickness of the samples were calculated using ImageJ (NIH, USA).

Mechanical Characterization. The viscoelastic properties of the polymer hydrogels and nanocomposites were analyzed by a MCR rheometer (Anton Paar, USA) using a 10 mm flat geometry. Time-dependent storage and loss moduli (G' and G'') were obtained by subjecting the material to 1% strain at 10 rad/s. The UV light was turned on after 30 s and kept on until the moduli were stabilized (180 s). Strain sweep was performed where the material was subjected to 0.1–10% strain at 10 rad/s, and the respective stress response was obtained from the sample.

Optical Setup. The Brillouin spectrometer follows the experimental setup is shown in Figure S1. A 532 nm single-frequency laser (GMSL-532-100FHA) with center wavelength (531.9587 nm ± 0.3 pm), nominal output line width (~640 kHz), and maximum output power of 100 mW was obtained from Lasermate Inc. Unwanted optical feedback from the setup was prevented using an optical isolator (BB-8-05-I-090) obtained from Electro-Optics Technology. The backscattered light was directed toward a confocal pinhole by placing a polarizing beam splitter along the beam path. A microscope objective lens was used to focus the pump onto the sample and to collect the backscattered light. To rotate the polarization of the back-reflected beam by 90°, we placed a Faraday optical rotator (Electro-Optics Technology, Inc.) before the objective lens. The backscattered beam was split by a long-pass filter and sent to a conventional Raman spectrometer and a VIPA spectrometer (for Brillouin spectra analysis). The sample was not damaged by incident radiation during experiments as the power was less than 40 mW.

The VIPA spectrometer followed the design set forth by Scarcelli *et al.*¹⁴ The input beam was coupled into an iodine absorption cell heated to ~130 °C (Figure S2). The undesired molecular emission and remaining Raman signal were filtered using a 532 nm line filter. When probing the pure GelMA hydrogels, the laser emission wavelength corresponds to the absorption line #660 of the iodine molecules according to Simmons and Hougen.²⁸ Therefore, the anti-Stokes peaks as shown in Figure 1e were partially absorbed by the iodine molecules. Because of this, we utilized the Stokes peaks for the purpose of retrieving the Brillouin shifts. Nevertheless, when probing the GelMA + HAP hydrogels, the laser was repaired and its emission wavelength hopped to another value (absorption line #642, according to Simmons

and Hougen²⁸), and we selected anti-Stokes peaks to retrieve the Brillouin shifts.

Determination of Brillouin Shift. In this study, we determined the Brillouin shift through an empirical method. We followed the paraxial approximations for both air-spaced and solid-spaced VIPAs reported in previous reports.^{29,30} The output at focal plane can be expressed as

$$A(\lambda, r) = \frac{1}{1 + F \sin^2 \left(\frac{nk}{2} \left(2d \cos \theta_t - \frac{2dr \tan \theta_t \sqrt{1 - n^2 \sin^2 \theta_t}}{n f_L} - \frac{dr^2 \cos \theta_t}{n f_L^2} \right) \right)} \\ = \frac{1}{1 + a \sin^2(b - d(r + r_0) - e(r + r_0)^2)} \quad (1)$$

θ_t is solely dependent on the tilting angle of the VIPA. Usually, the tilting angle is less than 1°; a , b , d , e , and r_0 are empirical parameters. Here, r_0 is the overall shift of the CCD camera (compared to the center of the periodical structures). Therefore, the positions of the elastic peaks will satisfy the following condition:

$$\nu_e(b + d(r + r_0) + e(r + r_0)^2) = (m + l)\pi \quad (2)$$

Here, m and l are both integers. In this particular case, $m = c/(\lambda \times \text{FSR}) \approx 16934$, and $l = 0, 1, 2, \dots$ (c is the light speed).

A typical Brillouin spectrum is given in Figure S3b. The Brillouin peaks are present beside the elastic peaks. The position and the line width of the peaks can be determined using a nonlinear fitting algorithm. We used Lorentzian function to fit the peaks, according to eq 1. In this way, the distance between the elastic peak and the neighboring Brillouin peak, Δr , can be determined. The Brillouin shift ν_B can be simplified according to the following expression:

$$\Delta \nu = \frac{(m + l)\pi}{b + d(r + \Delta r + r_0) + e(r + \Delta r + r_0)^2} - \nu_e \\ = \frac{(m + l)\pi}{b + d(r + \Delta r + r_0) + e(r + \Delta r + r_0)^2} \\ - \frac{(m + l)\pi}{b + d(r + r_0) + e(r + r_0)^2} \\ \approx B\Delta r + C\Delta r^2 + D\Delta r^3 + \dots \quad (3)$$

This expression can be expanded into Taylor series because $\Delta \nu$ is usually much smaller than ν_e . Based on the spacing of the elastic peaks, we know Δr when $\Delta \nu$ is integer multiples of the free spectral range (FSR) of the VIPA. For example, the spatial and the spectral distances between peaks 1 and 2 in Figure S3a are r_{21} and $\text{FSR} = 33.334$ GHz, respectively. Similarly, for peaks 1 and 3, their spatial distance is $r_{31} + r_{32}$, whereas their spectral distance is $2 \times \text{FSR} = 66.668$ GHz. Based on these data, we can solve the parameters B , C , D , ... in eq 3. Practically, the distances between different peaks are expressed in pixel numbers. In our experiment, the pixel number is 1600 using full vertical binning setup. An example pixel–spectral correspondence is shown in Figure S3b. Here, we used all four elastic peaks (the central peaks of the triplet structures) to determine the correspondence curve.

Statistical Analysis. The data are presented as mean ± standard deviation. One-way analysis of variance with Tukey's posthoc test for pairwise comparison was performed to obtained statistical difference between samples. Statistical significance is designated with * $p < 0.05$.

ASSOCIATED CONTENT

Supporting Information

The Supporting Information is available free of charge on the ACS Publications website at DOI: 10.1021/acsnano.6b08526.

Details of the experimental optical setup for Brillouin and Raman spectroscopy and microscopy; additional characterizations of nanostructured hydrogels using Brillouin and Raman, such as time-dependent measurements and

correlation between Brillouin spectroscopy and shear rheology (PDF)

AUTHOR INFORMATION

Corresponding Authors

*E-mail: gaharwar@tamu.edu.

*E-mail: yakovlev@tamu.edu.

ORCID

Akhilesh K. Gaharwar: 0000-0002-0284-0201

Vladislav V. Yakovlev: 0000-0002-4557-1013

Notes

The authors declare no competing financial interest.

ACKNOWLEDGMENTS

We acknowledge the support of the National Science Foundation (CBET Award 1250363, DBI Awards 1455671 and 1532188, and ECCS Award 1509268), the U.S. Department of Defense (DOD) (FA9550-15-1-0517), and the National Institutes of Health (R03 EB023454).

REFERENCES

- (1) Dvir, T.; Timko, B. P.; Kohane, D. S.; Langer, R. Nanotechnological Strategies for Engineering Complex Tissues. *Nat. Nanotechnol.* **2011**, *6*, 13–22.
- (2) Gaharwar, A. K.; Peppas, N. A.; Khademhosseini, A. Nanocomposite Hydrogels for Biomedical Applications. *Biotechnol. Bioeng.* **2014**, *111*, 441–453.
- (3) Kloxin, A. M.; Kloxin, C. J.; Bowman, C. N.; Anseth, K. S. Mechanical Properties of Cellularly Responsive Hydrogels and Their Experimental Determination. *Adv. Mater.* **2010**, *22*, 3484–3494.
- (4) Anseth, K. S.; Bowman, C. N.; Brannon-Peppas, L. Mechanical Properties of Hydrogels and Their Experimental Determination. *Biomaterials* **1996**, *17*, 1647–1657.
- (5) Tian, B.; Cohen-Karni, T.; Qing, Q.; Duan, X.; Xie, P.; Lieber, C. M. Three-dimensional, Flexible Nanoscale Field-effect Transistors as Localized Bioprobes. *Science* **2010**, *329*, 830–834.
- (6) Kim, K.; Jeong, C. G.; Hollister, S. J. Non-invasive Monitoring of Tissue Scaffold Degradation Using Ultrasound Elasticity Imaging. *Acta Biomater.* **2008**, *4*, 783–790.
- (7) Fatemi, M.; Greenleaf, J. F. Ultrasound-stimulated Vibro-acoustic Spectrography. *Science* **1998**, *280*, 82–85.
- (8) Muthupillai, R.; Lomas, D.; Rossman, P.; Greenleaf, J.; Manduca, A.; Ehman, R. Magnetic Resonance Elastography by Direct Visualization of Propagating Acoustic Strain Waves. *Science* **1995**, *269*, 1854–1857.
- (9) Koski, K. J.; Akhenblit, P.; McKiernan, K.; Yarger, J. L. Non-invasive Determination of the Complete Elastic Moduli of Spider Silks. *Nat. Mater.* **2013**, *12*, 262–267.
- (10) Gubbiotti, G.; Carlotti, G.; Madami, M.; Tacchi, S.; Vavassori, P.; Socino, G. Setup of a New Brillouin Light Scattering Apparatus with Submicrometric Lateral Resolution and Its Application to the Study of Spin Modes in Nanomagnets. *J. Appl. Phys.* **2009**, *105*, 07D521.
- (11) Reiss, S.; Burau, G.; Stachs, O.; Guthoff, R.; Stolz, H. Spatially Resolved Brillouin Spectroscopy to Determine the Rheological Properties of the Eye Lens. *Biomed. Opt. Express* **2011**, *2*, 2144–2159.
- (12) Stephanidis, B.; Adichtchev, S.; Gouet, P.; McPherson, A.; Mermet, A. Elastic Properties of Viruses. *Biophys. J.* **2007**, *93*, 1354–1359.
- (13) Randall, J.; Vaughan, J. M.; Cusack, S. Brillouin Scattering in Systems of Biological Significance. *Philos. Trans. R. Soc., A* **1979**, *293*, 341–348.
- (14) Scarcelli, G.; Yun, S. H. Confocal Brillouin Microscopy for Three-dimensional Mechanical Imaging. *Nat. Photonics* **2008**, *2*, 39–43.
- (15) Traverso, A. J.; Thompson, J. V.; Steelman, Z. A.; Meng, Z.; Scully, M. O.; Yakovlev, V. V. Dual Raman-Brillouin Microscope for Chemical and Mechanical Characterization and Imaging. *Anal. Chem.* **2015**, *87*, 7519–7523.
- (16) Meng, Z.; Traverso, A. J.; Yakovlev, V. V. Background Clean-up in Brillouin Microspectroscopy of Scattering Medium. *Opt. Express* **2014**, *22*, 5410–5416.
- (17) Meng, Z.; Yakovlev, V. V. Optimizing Signal Collection Efficiency of the VIPA-based Brillouin Spectrometer. *J. Innovative Opt. Health Sci.* **2015**, *08*, 1550021.
- (18) Xavier, J. R.; Thakur, T.; Desai, P.; Jaiswal, M. K.; Sears, N.; Cosgriff-Hernandez, E.; Kaunas, R.; Gaharwar, A. K. Bioactive Nanoengineered Hydrogels for Bone Tissue Engineering: A Growth-Factor-Free Approach. *ACS Nano* **2015**, *9*, 3109–3118.
- (19) Nichol, J. W.; Koshy, S. T.; Bae, H.; Hwang, C. M.; Yamanlar, S.; Khademhosseini, A. Cell-laden Microengineered Gelatin Methacrylate Hydrogels. *Biomaterials* **2010**, *31*, 5536–5544.
- (20) Thakur, T.; Xavier, J. R.; Cross, L.; Jaiswal, M. K.; Mondragon, E.; Kaunas, R.; Gaharwar, A. K. Photocrosslinkable and Elastomeric Hydrogels for Bone Regeneration. *J. Biomed. Mater. Res., Part A* **2016**, *104*, 879–888.
- (21) Shin, S. R.; Bae, H.; Cha, J. M.; Mun, J. Y.; Chen, Y.-C.; Tekin, H.; Shin, H.; Farshchi, S.; Dokmeci, M. R.; Tang, S.; Khademhosseini, A. Carbon Nanotube Reinforced Hybrid Microgels as Scaffold Materials for Cell Encapsulation. *ACS Nano* **2012**, *6*, 362–372.
- (22) Shin, S. R.; Jung, S. M.; Zalabany, M.; Kim, K.; Zorlutuna, P.; Kim, S. B.; Nikkhah, M.; Khabiry, M.; Azize, M.; Kong, J.; Wan, K.-t.; Palacios, T.; Dokmeci, M. R.; Bae, H.; Tang, X.; Khademhosseini, A. Carbon-Nanotube-Embedded Hydrogel Sheets for Engineering Cardiac Constructs and Bioactuators. *ACS Nano* **2013**, *7*, 2369–2380.
- (23) Jaiswal, M. K.; Xavier, J. R.; Carrow, J. K.; Desai, P.; Alge, D.; Gaharwar, A. K. Mechanically Stiff Nanocomposite Hydrogels at Ultralow Nanoparticle Content. *ACS Nano* **2016**, *10* (1), 246–256.
- (24) Meng, Z.; Yakovlev, V. V. Precise Determination of Brillouin Scattering Spectrum Using a Virtually Imaged Phase Array (VIPA) Spectrometer and Charge-Coupled Device (CCD) Camera. *Appl. Spectrosc.* **2016**, *70*, 1356–1363.
- (25) Ortiz, S.; Siedlecki, D.; Grulkowski, I.; Remon, L.; Pascual, D.; Wojtkowski, M.; Marcos, S. Optical Distortion Correction in Optical Coherence Tomography for Quantitative Ocular Anterior Segment by Three-dimensional Imaging. *Opt. Express* **2010**, *18*, 2782–2796.
- (26) Fabry, B.; Maksym, G. N.; Butler, J. P.; Glogauer, M.; Navajas, D.; Fredberg, J. J. Scaling the Microrheology of Living Cells. *Phys. Rev. Lett.* **2001**, *87*, 148102.
- (27) Antonacci, G.; Foreman, M. R.; Paterson, C.; Török, P. Spectral Broadening in Brillouin Imaging. *Appl. Phys. Lett.* **2013**, *103*, 221105.
- (28) Simmons, J. D.; Hougen, J. T. Atlas of the IR Spectrum from 19 000 to 18 000 cm⁻¹. *J. Res. Natl. Bur. Stand., Sect. A* **1977**, *6*, 6.
- (29) Xiao, S.; Weiner, A. M.; Lin, C. A Dispersion Law for Virtually Imaged Phased-array Spectral Dispersers Based on Paraxial Wave Theory. *IEEE J. Quantum Electron.* **2004**, *40*, 420–426.
- (30) Xiao, S.; Weiner, A. M. An Eight-channel Hyperfine Wavelength Demultiplexer Using a Virtually Imaged Phased-Array (VIPA). *IEEE Photonics Technol. Lett.* **2005**, *17*, 372–374.